




Neutral delay differential equation model of an optically injected Kerr cavity

Andrei G. Vladimirov  and Daria A. Dolinina 
Weierstrass Institute, Mohrenstrasse 39, 10117 Berlin, Germany

 (Received 31 July 2023; accepted 11 January 2024; published 12 February 2024)

A neutral delay differential equation (NDDE) model of a Kerr cavity with external coherent injection is developed that can be considered as a generalization of the Ikeda map with second- and higher-order dispersion being taken into account. It is shown that this model has solutions in the form of dissipative solitons both in the low dissipation limit, where the model can be reduced to the Lugiato-Lefever equation (LLE), and beyond this limit, where the soliton is eventually destroyed by the Cherenkov radiation. Unlike the standard LLE, the NDDE model is able to describe the overlap of multiple resonances associated with different cavity modes.

DOI: [10.1103/PhysRevE.109.024206](https://doi.org/10.1103/PhysRevE.109.024206)

I. INTRODUCTION

Over the past few decades, optical frequency combs have found numerous applications in different fields of science and industry, including spectroscopy, optical ranging, metrology, searching for exoplanets, microwave photonics, and optical communications [1–6]. Standard methods of frequency comb generation are based on the use of mode-locked lasers [7], optical microcavities subject to an external coherent injection [8], and electro-optical modulators [9]. A simple map to describe an injected Kerr cavity was proposed by Ikeda [10]. However, his model neglects the chromatic dispersion of the intracavity media, and therefore it is not applicable to describe such phenomena as dissipative soliton formation.

One of the most commonly used methods to model dispersive Kerr optical cavities is based on the application of the paradigmatic Lugiato-Lefever equation (LLE) [11], which is known to exhibit S-shaped branches of continuous wave (CW) solutions as well as temporal cavity solitons (TCSs) preserving their shape in the course of propagation along the cavity axis and sitting on a constant intensity background. Temporal dissipative solitons were observed experimentally in optical fiber cavities [12], mode-locked lasers [13], and optical microresonator frequency comb generators [14]. The LLE based on the mean-field approximation is, however, not free from certain shortcomings. In particular, it describes bistable behavior and TCS formation only in the vicinity of a single cavity resonance [14–16]. To overcome this limitation, the modeling approaches based on the infinitely dimensional Ikeda map [17,18] and a generalized LLE model with localized injection and losses [19,20] were developed to describe the appearance of the overlap of multiple nonlinear resonances, multistability of CW solutions, and supersolitons [18,21]. Here we propose an alternative approach to model nonlinear dynamics of an injected Kerr cavity based on a second-order neutral-type delay differential equation (NDDE), which also can be considered as a generalization of the Ikeda map [10]. We show that in a certain limit, the NDDE model can be reduced to the LLE.

We perform a linear stability analysis of the NDDE model in the practically important large delay limit, and we present numerical evidence of the existence of stationary and oscillating dissipative optical solitons in it. Beyond the LLE limit, the TCSs of the NDDE model are strongly affected by Cherenkov radiation induced by high-order dispersion [22]. The modeling approach proposed here can be adopted to study the dynamics of solid state and fiber lasers, where the chromatic dispersion of the intracavity media plays an important role in the mechanism of the short pulse generation, as well as to investigate the effect of second- and higher-order dispersion on the characteristics of mode-locking regimes in semiconductor lasers. Furthermore, the NDDE model might be useful to model the coupled-cavity systems such as a microcavity optical frequency comb generator pumped by a semiconductor mode-locked light source, which is already successfully modeled by DDE models [23–26].

II. MODEL EQUATION

Time-delay equations have proven to be an efficient tool for modeling nonlinear dynamics of lasers with feedback [27], coupled laser systems [28], mode-locked lasers [23,29,30], as well as long cavity laser devices [31,32]. However, unlike the mean-field models such as LLE and Haus master equation, where chromatic dispersion is modeled by time derivatives, the inclusion of intracavity dispersion in DDE laser models is not as straightforward. Several methods to account for dispersion in DDE models were proposed in Refs. [33–39]. In particular, in Ref. [39] the first-order neutral delay differential equation (NDDE) was developed to describe Gires-Tournois interferometer in the conservative limit. A NDDE is a differential equation with the highest order derivative of the unknown function appearing with both nondelayed argument t and delayed argument $t - \tau$. The advantage of the model of Ref. [39] is that similarly to mean-field models, the time derivative terms in it describe the chromatic dispersion only and do not introduce additional dissipation. Here we propose a second-order NDDE model of a ring Kerr cavity subject to

a coherent optical injection:

$$\begin{aligned} & \left(A + a\partial_t A + \frac{a^2 - ib}{2} \partial_{tt} A \right) e^{-i\alpha|A|^2/2 - i\theta/2} \\ &= \sqrt{\kappa} \left(A_\tau - a\partial_t A_\tau + \frac{a^2 + ib}{2} \partial_{tt} A_\tau \right) e^{i\alpha|A_\tau|^2/2 + i\theta/2} + \eta. \end{aligned} \quad (1)$$

Here t is the time, $A(t)$ is the normalized complex electric field envelope, and $A_\tau = A(t - \tau)$ is the retarded field amplitude with the delay parameter $\tau = nL/c$ equal to the linear round-trip time of the cavity, where L is the cavity length, n is the averaged intracavity refractive index, and c is the velocity of light. α is the Kerr coefficient, η is the injection parameter, $\eta = \sqrt{T}E_i$, where E_i is the input field envelope and T is the intensity coupling coefficient [40], θ describes the detuning between the injection frequency and the frequency of a cavity mode, and $\kappa < 1$ is the linear intensity attenuation factor per cavity round-trip due to internal and coupling losses. The coefficients $a > 0$ and b are responsible for the intracavity dispersion. Here $b > 0$ corresponds to the regime of anomalous dispersion. Note that, as will be shown below, in the LLE limit only the coefficient b contributes to the second-order dispersion, while the parameter a describes the group delay due to the first-order dispersion. The derivation of the model (1) is given in the next section.

In the absence of injection and losses, $\eta = 0$ and $\kappa = 1$, the linear part of Eq. (1) is similar to that of the conservative version of the Gires-Tournois interferometer model introduced in [39]. Similarly to this model, Eq. (1) with $\eta = 0$ and $\kappa = 1$ is symmetric under the transformation $t \rightarrow -t$ and $A \rightarrow A^*$ combined with the time shift, hence it is reversible in the nondissipative limit. Note, however, that unlike the first-order NDDE Gires-Tournois interferometer model studied in [39], the second-order derivative terms responsible for the second-order dispersion in the LLE limit are present in Eq. (1); see also Ref. [38]. This is an important difference between Eq. (1) and the model of Ref. [39]. Note that for $a = b = 0$, Eq. (1) becomes similar to the well-known Ikeda map [10]. The derivation of Eq. (1) is given in the next section together with the derivation of two other versions of the NDDE model including the mean-field one. An advantage of the model equation (1) is that in the nondissipative limit, $\eta = 0$ and $\kappa = 1$, similarly to the first-order NDDE discussed in [39], it admits a relatively simple conserved quantity $\partial_t W(t) = 0$ with

$$\begin{aligned} W(t) &= a^3 |\partial_t A|^2 + ib(A\partial_t A^* - A^*\partial_t A) + 2a|A|^2 \\ &+ \int_t^{t+\tau} \left| A(x) + a\partial_x A(x) + \frac{a^2 - ib}{2} \partial_{xx} A(x) \right|^2 dx. \end{aligned} \quad (2)$$

III. MODEL DERIVATION

To derive the NDDE model, let us consider the schematic representation of a ring Kerr cavity with a pair of thin dispersive elements and two identical Kerr media shown in Fig. 1. The field envelope on the output of the left Kerr medium is given by $A_2(t + \tau_1) = A_1(t)e^{i\alpha|A_1(t)|^2/2 + i\phi_1}$, where α is the Kerr

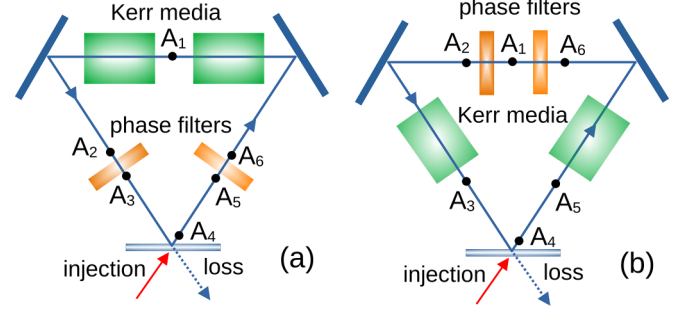


FIG. 1. Ring cavity with two Kerr media (green) and a pair of identical thin dispersive elements (orange). Cavity schemes in (a) and (b) are used to derive Eqs. (7) and (1), respectively.

coefficient, and ϕ_1 and τ_1 are the phase shift and the delay time due to the propagation in the cavity; see Fig. 1(a).

The Fourier transform of the field envelope at the output from a thin dispersive element (phase filter) is given by $\hat{A}_3(\omega) = \hat{f}(\omega)\hat{A}_2(\omega)$, where $\hat{A}_2(\omega)$ is the Fourier transform of the input field $A_2(t)$ and $\hat{f}(\omega) = e^{i\Phi(\omega)}$ with real $\Phi(\omega)$; see, e.g., Ref. [33]. Close to $\omega = 0$ we can use the expansion

$$\begin{aligned} \hat{f}(\omega) &= e^{i\Phi(0)} \{ 1 + i\omega\Phi'(0) \\ &- [\Phi'(0)^2 - i\Phi''(0)]\omega^2/2 + O(\omega^3) \}. \end{aligned} \quad (3)$$

Taking this relation into account, the electric field envelope A_3 can be expressed as

$$\begin{aligned} A_3(t) &= \mathcal{F}^{-1}[\hat{f}(\omega)\hat{A}_2(\omega)] \\ &= \mathcal{F}^{-1} \left\{ e^{i\phi/2} \left[1 + i\omega a - \frac{a^2 + ib}{2} \omega^2 + O(\omega^3) \right] \hat{A}_2(\omega) \right\} \\ &= \left[1 - a\partial_t + \frac{a^2 + ib}{2} \partial_{tt} + O(\partial_{ttt}) \right] A_2(t) e^{i\phi/2}, \end{aligned} \quad (4)$$

where \mathcal{F}^{-1} is the inverse Fourier transform, $\Phi(0) \equiv \phi/2$ is the phase shift, $\Phi'(0) \equiv a$ is the group delay parameter, and $\Phi''(0) \equiv -b$ is the second-order dispersion coefficient. The field amplitude A_4 is obtained from A_3 by taking into account time delay τ_2 , phase shift ϕ_2 , and introducing the injection η and the intensity attenuation factor κ due to the cavity losses. Thus we get

$$\begin{aligned} A_4\left(t + \frac{\tau}{2}\right) &= \sqrt{\kappa} \left[1 - a\partial_t + \frac{a^2 + ib}{2} \partial_{tt} + O(\partial_{ttt}) \right] \\ &\times A_1 e^{i\alpha|A_1|^2/2 + i\theta/2} + \eta, \end{aligned} \quad (5)$$

with one-half of the cavity round trip time $\tau/2 = \tau_1 + \tau_2$ and the phase shift $\theta/2 = (\phi_1 + \phi/2 + \phi_2)$.

The field envelope on the input of the left Kerr medium is given by $A_6(t - \tau_1) = A_1(t)e^{-i\alpha|A_1(t)|^2/2 - i\phi_1}$ with $|A_1(t)|^2 = |A_6(t - \tau_1)|^2$. The Fourier transform of the field envelope A_6 is given by $\hat{A}_6(t) = \hat{f}(\omega)\hat{A}_5(\omega)$, which can be rewritten as $\hat{A}_5(t) = \hat{f}^{-1}(\omega)\hat{A}_6(\omega) = \hat{f}^*(\omega)\hat{A}_6(\omega)$. Hence we get

$$\begin{aligned} A_5(t) &= \mathcal{F}^{-1}[\hat{f}^*(\omega)\hat{A}_6(\omega)] \\ &= \left[1 + a\partial_t + \frac{a^2 - ib}{2} \partial_{tt} + O(\partial_{ttt}) \right] A_6(t) e^{-i\phi/2}. \end{aligned}$$

Therefore, similarly to (5), we obtain

$$A_4\left(t - \frac{\tau}{2}\right) = \left[1 + a\partial_t + \frac{a^2 - ib}{2}\partial_{tt} + O(\partial_{ttt})\right] \times A_1 e^{-i\alpha|A_1|^2/2 - i\theta/2}. \quad (6)$$

Finally, shifting the time in Eq. (5) by $-\tau$, equating the resulting equation to Eq. (6), and neglecting high-order terms $O(\partial_{ttt})$, we get

$$\begin{aligned} & \left(1 + a\partial_t + \frac{a^2 - ib}{2}\partial_{tt}\right) A e^{-i\alpha|A|^2/2 - i\theta/2} \\ &= \sqrt{\kappa} \left(1 - a\partial_t + \frac{a^2 + ib}{2}\partial_{tt}\right) A_\tau e^{i\alpha|A_\tau|^2/2 + i\theta/2} + \eta, \end{aligned} \quad (7)$$

where $A \equiv A_1$ and $A_\tau = A(t - \tau)$.

The model (1) can be derived in a similar way to Eq. (7). For the scheme shown in Fig. 1(b), we get

$$A_2 \approx A_1 - a\partial_t A_1 + \frac{a^2 + ib}{2}\partial_{tt} A_1 \quad (8)$$

and

$$A_4\left(t + \frac{\tau}{2}\right) \approx \sqrt{\kappa} A_2 e^{i\alpha|A_2|^2/2 + i\theta/2} + \eta. \quad (9)$$

Here, the approximate equality sign means that we have neglected the high-order terms $O(\partial_{ttt})$. Substituting Eq. (8) into Eq. (9), assuming that a , b , and α are sufficiently small, and neglecting the $O(\alpha a)$ and $O(\alpha b)$ terms in the exponential, we obtain

$$A_4\left(t + \frac{\tau}{2}\right) \approx \sqrt{\kappa} \left(A_1 - a\partial_t A_1 + \frac{a^2 + ib}{2}\partial_{tt} A_1\right) \times e^{i\alpha|A_1|^2/2 + i\theta/2} + \eta. \quad (10)$$

Similarly, for another half of the cavity, we get

$$A_4\left(t - \frac{\tau}{2}\right) \approx \left(A_1 + a\partial_t A_1 + \frac{a^2 - ib}{2}\partial_{tt} A_1\right) \times e^{-i\alpha|A_1|^2/2 - i\theta/2}. \quad (11)$$

Finally, combining Eqs. (10) and (11), we arrive at the NDDE model (1).

In the mean-field approximation, where the field amplitude is small, expanding the exponential functions in Eq. (1) we get the following equation:

$$\begin{aligned} & \left(A + a\partial_t A + \frac{a^2 - ib}{2}\partial_{tt} A - i\frac{\alpha}{2}A|A|^2\right) e^{-i\theta/2} \\ &= \sqrt{\kappa} \left(A_\tau - a\partial_t A_\tau + \frac{a^2 + ib}{2}\partial_{tt} A_\tau + i\frac{\alpha}{2}A_\tau|A_\tau|^2\right) \\ & \times e^{i\theta/2} + \eta. \end{aligned} \quad (12)$$

Neutral DDEs (1), (7), and (12) are reversible in the nondissipative limit $\eta = 0$ and $\kappa = 1$. This property is similar to that of the LLE, which will be derived from these equations in the next section. As will be shown in the next section, the parameter b corresponds to the second-order dispersion coefficient in the LLE limit. In the absence of second-order

dispersion, $b = 0$, according to Eq. (8) the field amplitude on the output of the dispersive element is defined by

$$A_2 \approx A_1 - a\partial_t A_1 + \frac{a^2}{2}\partial_{tt} A_1 = A_1(t - a) + O(a^3).$$

Therefore, the parameter a has the meaning of the group delay introduced by the dispersive element. The inequality $a > 0$ follows from the causality principle. As will be shown below, this inequality is the necessary but not sufficient condition of the absence of a spurious instability in the NDDE models.

Note that a straightforward derivation of the model equation without splitting Kerr and dispersive media into two symmetric parts would result in a ‘‘regular’’ DDE model instead of NDDE:

$$\begin{aligned} & A + 2a\partial_t A + (2a^2 - ib)\partial_{tt} A \\ &= \sqrt{\kappa} A(t - \tau) e^{i\alpha|A(t - \tau)|^2 + i\theta} + \eta, \end{aligned} \quad (13)$$

which is similar to the generalization of the Ikeda map derived in [38] to describe a Kerr cavity with two spectral filters. After rescaling the time variable $t \rightarrow \sqrt{2}at$, the DDE model (13) becomes a particular case of Eq. (12) from Ref. [38] with the coefficient $\sqrt{2}$ in front of the first derivative instead of the coefficient σ in Eq. (12) of Ref. [38]. However, it was shown in Ref. [38] that the relation $\sigma = \sqrt{2}$ contradicts the applicability condition of the DDE model derived in this paper. Below, in Sec. V we show that Eq. (13) with $b \neq 0$ demonstrates a spurious instability in the nondissipative limit, $\kappa = 1$ and $\eta = 0$. This instability is related to a spurious dissipation (spectral filtering) introduced by the truncation of the series expansion in Eq. (3). On the other hand, in the derivation of the NDDE model (1) we have used two symmetric truncations of the two identical transfer functions, and in this case the corresponding dissipative contributions cancel each other. Therefore, only symmetric schemes such as those shown in Fig. 1 allow us to eliminate unphysical dissipation and spurious instability from the model equations.

To conclude this section, we note that the derivation presented here can be trivially generalized by including higher-order derivative terms in the model equation.

IV. REDUCTION TO THE LLE

Using the multiscale method described in [41], we can derive the same LLE from any one of the three model equations (1), (7), and (12). To be more specific, we choose Eq. (1), and in the large delay limit $\tau = \tau_0 \epsilon^{-1}$ with $\epsilon \ll 1$ and $\tau_0 = O(1)$ we rescale the time as $x = \epsilon t$ to get

$$\begin{aligned} & \left(A' + \epsilon a\partial_x A' + \epsilon^2 \frac{a^2 - ib}{2}\partial_{xx} A'\right) e^{-i\alpha|A'|^2/2 - i\theta/2} \\ &= \sqrt{\kappa} \left(A'_{\tau_0} - \epsilon a\partial_x A'_{\tau_0} + \epsilon^2 \frac{a^2 + ib}{2}\partial_{xx} A'_{\tau_0}\right) \\ & \times e^{i\alpha|A'_{\tau_0}|^2/2 + i\theta/2} + \eta, \end{aligned} \quad (14)$$

where $A'_{\tau_0} = A'(x - \tau_0) = A(t - \tau)$. Next, we introduce two timescales $A'(x) = u(t_0, t_2)$, where $t_0 = (1 - \epsilon c_1 + \epsilon^2 c_2 + \dots)x$, $t_2 = \epsilon^2 x / \tau_0$, and we rescale the parameters as

$$\alpha = \epsilon^2 \chi, \quad \kappa = e^{-2\epsilon^2}, \quad \eta = \epsilon^2 r. \quad (15)$$

Substituting these expressions into Eq. (14), collecting the first-order terms in ϵ , and using the Fredholm alternative, we obtain the following boundary condition:

$$u(t_0, t_2) = u(t_0 - \tau_0, t_2)e^{i\theta}, \quad (16)$$

together with the relation $c_1 = 2a/\tau_0$ for the group delay parameter. Finally, collecting the second-order terms in ϵ , we get $c_2 = 4a^2/\tau_0^2$ and an equation similar to LLE, but with the detuning parameter entering boundary condition (16) rather than the equation itself:

$$\partial_{t_2} u = -u + i\chi u|u|^2 + ib\partial_{t_0} u + r. \quad (17)$$

Note that Eq. (17) with the boundary condition (16), where the parameter θ plays the role of the detuning, is able to describe multiple resonances corresponding to different cavity modes. However, it cannot describe the overlap of these resonances. To get overlapping resonances and coexisting different solitons, one needs to replace distributed injection and losses with the localized ones, as was proposed in [19]. It is seen from Eq. (17) that the coefficient b in front of the second derivative terms is responsible for the second-order dispersion in the LLE limit; see also [38]. Therefore, these derivatives cannot be neglected in the model equation.

Using the additional assumption that the detuning is small,

$$\theta = -\epsilon^2 \Theta, \quad (18)$$

instead of (17) we get standard LLE describing a vicinity of a single cavity resonance,

$$\partial_{t_2} u = -u - i\Theta u + i\chi u|u|^2 + ib\partial_{t_0} u + r, \quad (19)$$

with the periodic boundary condition $u(t_0, t_2) = u(t_0 - \tau_0, t_2)$.

Note that, unlike Eqs. (17) and (19) obtained by collecting ϵ^2 -terms, in Ref. [39], where the nonlinear Schrödinger equation (NLSE) was derived from a NDDE without second-order derivatives and the external injection, the second- and third-order dispersion terms appear simultaneously in the order ϵ^3 . The NLSE is then obtained by choosing the detuning in such a way that the third-order dispersion vanishes. In the conservative limit, the LLE (19) also transforms into the NLSE. However, the existence of stable soliton solutions is hardly possible in the original NDDE model near this limit. Unlike the standard NLSE, the NDDE contains the dispersion of all the orders. This can be easily understood by taking into account that in Eq. (3) we expand in power series the exponential $e^{i\Phi(\omega)}$, not just $\Phi(\omega)$. For example, in the case in which only first- and second-order dispersion terms $a\omega$ and $b\omega^2/2$ are present in $\Phi(\omega)$, all orders of ω appear in the expansion of $e^{i\Phi(\omega)}$. Therefore, the truncation of such high-order terms made in the course of the derivation of the NDDE model introduces high-order dispersion into it; see also Ref. [39], where the first-order derivatives are responsible for the appearance of third-order dispersion in the model equation. On the other hand, it is well known that the solitons of the NLSE are destroyed by the Cherenkov radiation [42,43] in the presence of an arbitrary small third-order dispersion term [44–46].

As was already mentioned above, the parameter ϵ describes the distance from the LLE (mean-field) limit, and it can be expressed in terms of the attenuation factor κ using Eq. (15), $\epsilon = \sqrt{-\ln \kappa/2}$. In particular, in the case of high-finesse cavity

and weak coupling, $1 - \kappa \ll 1$, we get $\epsilon \approx \sqrt{(1 - \kappa)/2} \ll 1$, which means that at moderate injections the dynamics of such cavities can be described by the LLE, and all three NDDE models, (1), (7), and (12), are roughly equivalent. Nevertheless, even in this case, the NDDE models may be more convenient than the LLE when considering the coupling between microcavities and laser light sources. Assuming that the coupling losses dominate over the internal ones and the coupling is symmetric, the finesse can be estimated as $F \approx \pi/(1 - \kappa)$ [47]. Using this relation together with Eq. (15), we get $\epsilon \approx 0.0125$ for $F \approx 10^4$. On the other hand, in Ref. [21] experimental observation of super solitons was reported in a 100-m-long fiber cavity with much smaller finesse, $F \approx 20$. The LLE and the cubic NDDE (12) having not more than three CW solutions are not suitable for the description of these solitons. The remaining two NDDE models, (1) and (7), differ only by the relative position of the dispersive elements and dissipation (cavity losses and injection). This difference might be meaningful only when considering the effect of localized dispersion on the dynamics of the optical cavity; see, e.g., Ref. [33], where a photonic crystal mode-locked laser was discussed. Below we mainly concentrate on the analysis of the simpler Eq. (1) of the two models, (1) and (7), capable of describing the overlap of the cavity resonances.

V. STABILITY ANALYSIS IN THE LINEAR CONSERVATIVE LIMIT

Let us consider the equation

$$A + a\partial_t A + \frac{a^2 - ib}{2}\partial_{tt} A = \left(A_\tau - a\partial_t A_\tau + \frac{a^2 + ib}{2}\partial_{tt} A_\tau \right) e^{i\theta}, \quad (20)$$

obtained by the linearization of the NDDE models with $\kappa = 1$ and $\eta = 0$ at the trivial solution $A = 0$. Substituting $A(t) = A_0 e^{\lambda t}$ into (20), we get the characteristic equation

$$1 + a\lambda + \frac{a^2 - ib}{2}\lambda^2 = \left(1 - a\lambda + \frac{a + ib}{2}\lambda^2 \right) e^{-\lambda\tau + i\theta}. \quad (21)$$

In the large delay limit using the approach of Ref. [48], we substitute $e^{-\lambda\tau} \equiv Y(\lambda)$ into Eq. (21), solve the resulting equation with respect to $Y(\lambda)$, and set $\lambda = iv$. Thus, we get the following expression for the pseudocontinuous spectrum in the limit $\tau \rightarrow \infty$,

$$\begin{aligned} \lambda\tau &= -\ln \left[\frac{1 + iav - (a^2 - ib)v^2/2}{1 - iav - (a^2 + ib)v^2/2} e^{-i\theta} \right] \\ &= -\ln e^{i\Psi(v) - i\theta} = -i\Psi(v) + i\theta \end{aligned} \quad (22)$$

with real $\Psi(v)$. The fact that the pseudocontinuous spectrum of Eq. (20) is purely imaginary is obviously a consequence of the reversibility of this equation; see also Ref. [39]. However, whether this equation exhibits spurious instability depends on the discrete spectrum of the characteristic equation (21). In the large delay limit, discrete eigenvalues with positive (negative) real parts correspond to small $|Y(\lambda)| \ll 1$ [large $|Y(\lambda)| \gg 1$] in the limit $\tau \rightarrow \infty$. Therefore, they can be obtained by equating to zero the left (the expression in the brackets in

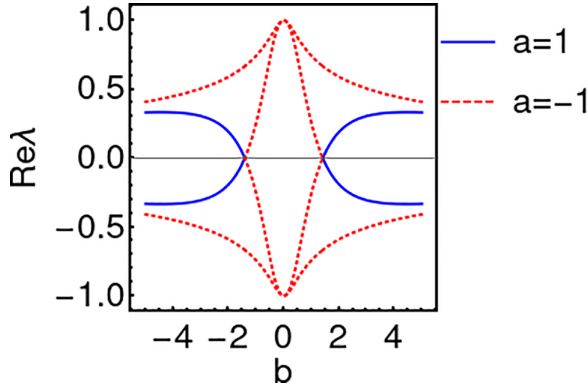


FIG. 2. Real parts of discrete eigenvalues for $a = 1$ (blue line) and $a = -1$ (red dotted line).

the right -hand side of Eq. (21), $1 + a\lambda + (a^2 - ib)\lambda^2/2 = 0$ [$1 - a\lambda + (a^2 + ib)\lambda^2/2 = 0$], which gives

$$\lambda_{\pm} = \frac{-a \pm \sqrt{-a^2 + 2ib}}{a^2 - ib} \quad (23)$$

for the discrete eigenvalues with positive real parts. The discrete eigenvalues with negative real parts are obtained from (23) by changing the signs of a and b . The real parts of the discrete eigenvalues are shown in Fig. 2 as functions of the “second-order dispersion coefficient” b . It is seen that for $a < 0$ one of the two discrete eigenvalues always has a positive real part. This means that Eq. (20) with $a < 0$ should demonstrate a spurious instability. For $a > 0$ there are no discrete eigenvalues if

$$|b| < \sqrt{2}a^2. \quad (24)$$

Hence, in order to avoid spurious instabilities below we choose $a > 0$ in the NDDE models and assume that the inequality (24) is satisfied. Note that positive coefficient a can be rescaled to unity by rescaling the time variable in the model equations.

Some results of numerical simulations of the linear conservative system (20) are shown in Fig. 3. Two left panels in this figure correspond to the parameter values satisfying the condition (24). Here the initial Gaussian pulse is gradually

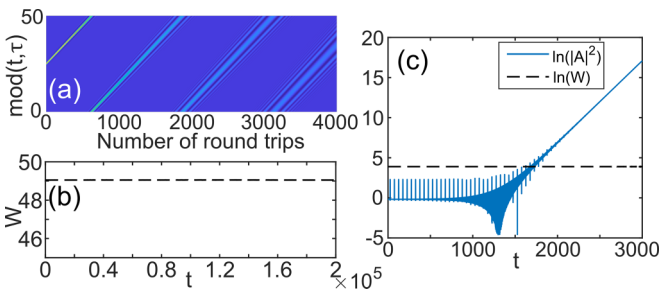


FIG. 3. Dynamics of the linear conservative system (20) with $a = \epsilon$, $\theta = -3.5\epsilon^2$, $\epsilon = 0.02$, $\tau = 50$. Panels (a) and (b) correspond to $b = \epsilon^2$ when the inequality (24) is satisfied and spurious instability is absent. Panel (c) illustrates on logarithmic scale spurious instability obtained for $b = 1.4143\epsilon^2 > \sqrt{2}a^2$. Horizontal dashed lines in panels (b) and (c) show that the integral $W(t)$ remains constant.

destroyed by the dispersion. The right panel illustrating the spurious instability is obtained for $b > \sqrt{2}a^2$. It is also seen from this panel that the integral defined by Eq. (2) remains constant when the instability develops.

Substituting $\kappa = 1$ and $\eta = 0$ into Eq. (13) and linearizing this equation at $A = 0$ instead of (22) we get $\lambda\tau = -\ln[1 + 2ia\nu - (2a^2 - ib)\nu^2] + i\theta$. In particular, at $\nu = 0$ one obtains

$$\text{Re}\lambda = \text{Re} \frac{d\lambda}{d\nu} = \text{Re} \frac{d^2\lambda}{d\nu^2} = 0, \quad \text{Re} \frac{d^3\lambda}{d\nu^3} = -\frac{3b}{\tau}.$$

It follows from these relations that for any nonzero b and sufficiently small ν the curve of the pseudocontinuous spectrum visits the right half-plane of the complex plane. Therefore, in this case one can expect an instability associated with the pseudocontinuous spectrum in the large delay limit.

In the analysis below, we consider only the case of anomalous dispersion, $b > 0$, where typical solutions of the LLE are bright dissipative solitons. A detailed bifurcation analysis of the NDDE model in normal and anomalous dispersion regimes will be addressed in our future work.

VI. CW SOLUTIONS

In this section, we study the linear stability of the CW solutions of Eq. (1). The amplitude A of the CW solutions satisfies the equation

$$Ae^{-i\alpha|A|^2/2 - i\theta/2} = \sqrt{\kappa}Ae^{i\alpha|A|^2/2 + i\theta/2} + \eta. \quad (25)$$

Substituting into Eq. (25) $A = \sqrt{I}e^{i\varphi}$, where I and φ are the intensity and the phase of the CW solution, and separating real and imaginary parts of the resulting equation, we get the following equation for the CW intensity:

$$[1 + \kappa - 2\sqrt{\kappa} \cos(\theta + \alpha I)]I = \eta^2, \quad (26)$$

which is transformed into the corresponding relation of the LLE in the limit (15) and (18). The phase of the CW solution is given by

$$\tan \varphi = \frac{\sin(\frac{\alpha I}{2}) + \sqrt{\kappa} \sin(\theta + \frac{\alpha I}{2})}{\cos(\frac{\alpha I}{2}) - \sqrt{\kappa} \cos(\theta + \frac{\alpha I}{2})}.$$

Nonlinear resonances of CW solutions of Eq. (1) near cusp bifurcations corresponding to different cavity modes are shown in Fig. 4(a).

The saddle-node bifurcations of the CW solutions are defined by the conditions

$$4\alpha^2\kappa I^4 - \alpha^2 I^2[\eta^2 - (\kappa + 1)I]^2 = \eta^4,$$

$$\theta_{\pm} = \arctan \left[\frac{-(1 + \kappa)\alpha I \pm \sqrt{\kappa(4\alpha^2 I^2 + 2 - \kappa) - 1}}{1 + \kappa \pm \alpha I \sqrt{\kappa(4\alpha^2 I^2 + 2 - \kappa) - 1}} \right] - \alpha I + 2\pi n,$$

where θ_{\pm} with $n = 0, \pm 1, \pm 2 \dots$ define pairs of saddle-node bifurcation curves originating from the cusp bifurcation points corresponding to different cavity resonances. Figure 4(b) illustrates the coexistence of multiple CW solutions of Eq. (1). It is seen that at sufficiently high injections, the CW resonances start overlapping. Unlike the resonances shown in

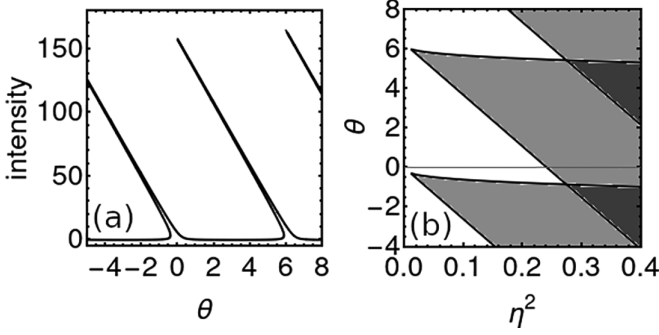


FIG. 4. Intensity of CW solutions of Eq. (1) as a function of the detuning parameter θ for $\eta = 0.5$ (a). Saddle-node bifurcations of CW solutions on the (η^2, θ) -plane (b). White, light gray, and dark gray areas limited by the saddle-node bifurcations indicate the existence of one, three, and five CW solutions, respectively. The parameter values, $\kappa = 0.923$ and $\alpha = 0.04$, correspond to $\epsilon = 0.2$ in Eq. (15).

Fig. 4(b), the resonances of Eq. (12) with cubic nonlinearity are much more narrow and never overlap. This can be easily understood by noticing that for cubic nonlinearity Eq. (26) transforms into a cubic equation in I having not more than three solutions. Hence, the mean-field model (12) does not describe well the dynamics of Eq. (1) beyond the LLE limit. Therefore, below we focus mainly on the model (1), which does not assume the mean-field approximation.

To study the linear stability of the CW solution, we linearize Eq. (1) around this solution, $A(t) = (\sqrt{I} + \delta A e^{\lambda t}) e^{i\varphi}$. This leads to the following characteristic equation:

$$c_2 Y^2 + c_1 Y + c_0 = 0, \quad (27)$$

where $Y(\lambda) = \exp(-\lambda\tau)$ and the coefficients $c_{0,1,2}$ are polynomials in λ :

$$\begin{aligned} c_2 &= \kappa + \frac{\kappa\lambda}{4} [(a^4 + b^2)\lambda^3 - 4a^3\lambda^2 + 2(4a^2 - b\alpha I)\lambda - 8a], \\ c_1 &= \frac{\sqrt{\kappa}}{2} \{ [(b^2 - a^4)\lambda^4 - 2b\alpha I\lambda^2 - 4] \cos(\alpha I + \theta) \\ &\quad + 2(2 + a^2\lambda^2)(\alpha I - b\lambda^2) \sin(\alpha I + \theta) \}, \\ c_0 &= \frac{1}{4} [(a^4 + b^2)\lambda^4 + 4a^3\lambda^3 + 2(4a^2 - b\alpha I)\lambda^2 + 8a\lambda + 4]. \end{aligned} \quad (28)$$

In the limit of large delay time $\tau \rightarrow \infty$, the eigenvalues of the pseudocontinuous spectrum can be represented as $\lambda \approx i\nu + \gamma/\tau$ with real ν and γ [48]. The pseudocontinuous spectrum is given by the two solution branches of the quadratic equation (27):

$$\gamma(\nu) = -\text{Re}[\ln |Y(i\nu)|]. \quad (29)$$

Stable CW solutions are characterized by $\gamma(\nu) < 0$ and, in particular, $\gamma(0) < 0$. At the saddle-node (flip) bifurcation point, we have $\gamma(0) = 0$ and $Y(0) = 1$ [$\gamma(0) = 0$ and $Y(0) = -1$], while modulational instability takes place when one or both branches of the pseudocontinuous spectrum are tangent to the imaginary axis at $\nu = \pm\nu_m$ with $|\nu_m| > 0$.

Some results of linear stability analysis of CW solutions Eq. (1) obtained for the parameter values far away from the

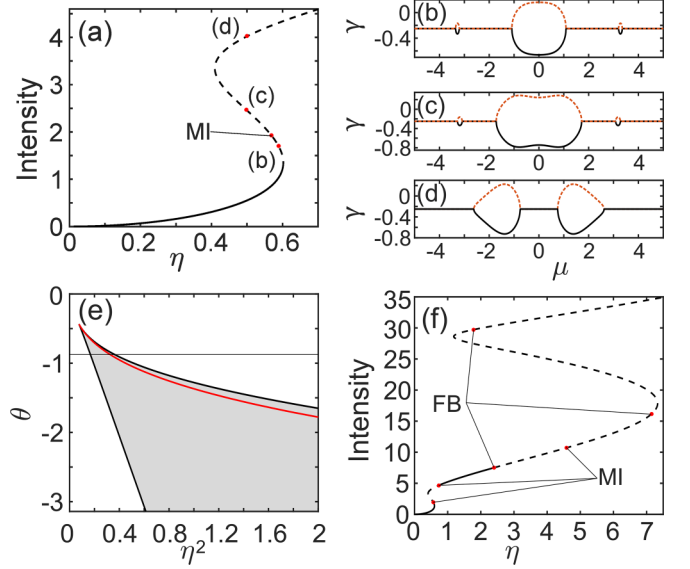


FIG. 5. S-shaped dependence of the intensity I of CW solutions on the injection rate η (a). Curves of pseudocontinuous spectrum for different values of I ; $I \approx 1.7032$ (b), $I \approx 2.4643$ (c), $I \approx 4.0221$ (d). Saddle-node bifurcations (black curves) and modulational instability (red curve) around a single cavity resonance on the (θ, η^2) -plane (e). CW solutions from panel (a) in the region of larger η and I (f). Parameters are $\epsilon = 0.5$, $\kappa = e^{-2\epsilon^2}$, $\alpha = \epsilon^2$, $\theta = -3.5\epsilon^2$, $a = \epsilon$, and $b = \epsilon^2$. In panels (a) and (f), unstable solutions are shown by dashed lines. MI (FB) indicates the modulational (flip) bifurcation points.

LLE limit, $\epsilon = 0.5$, are shown in Fig. 5. The S-shaped CW curve of Eq. (1) is shown in Fig. 5(a). It is seen that modulational instability takes place on the unstable middle part of the CW curve and destabilizes its upper part. Figures 5(b)–5(d) present the real parts of the pseudocontinuous eigenvalues $\gamma(\nu)$ calculated at the points indicated in Fig. 5(a). Figure 5(e) illustrates the location of the modulational instability curve between two saddle-node bifurcations around a single cavity resonance in the (η^2, θ) -plane. Finally, Fig. 5(f) illustrates a growing multiplicity of the solutions of Eq. (26) due to the overlap of resonances with increasing the injection.

It is important also to check the discrete spectrum of nonlinear CW solutions. The discrete spectrum is defined by the instantaneous part of the model equation, and it can be obtained by solving the equation $c_0 = 0$ with respect to λ , where c_0 is defined by Eqs. (27) and (28). It is seen from Fig. 6 corresponding to $b = (\sqrt{2} + 0.01)a^2$ that when b exceeds slightly the critical value defined by (24), the lower part of the CW branch can become unstable with respect to the discrete spectrum; see Fig. 6(a). The increase of the CW intensity I has a stabilizing effect on the discrete spectrum. However, as is seen from Fig. 6(b), the solution of Eq. (1) starting from the upper CW state becomes unbounded in the limit $t \rightarrow \infty$. This behavior might be attributed to a spurious instability.

Note that, as was shown in Sec. IV, when ϵ is small enough the NDDE model is equivalent to the LLE. Therefore, in this case it demonstrates the same bifurcation phenomena as described, e.g., in Ref. [49]. However, for sufficiently large ϵ and η the equivalence does not hold anymore. This is,

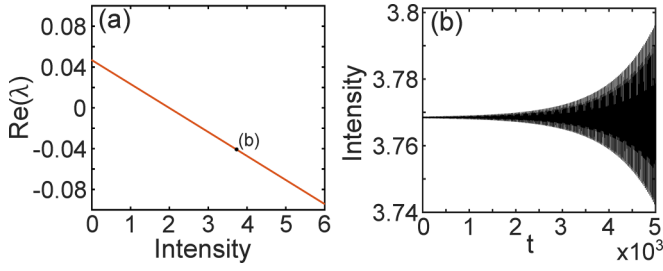


FIG. 6. Largest real part of the discrete eigenvalues of the CW solution with $b = (\sqrt{2} + 0.01)a^2$ as a function of the CW intensity I (a). $a = 0.1$. Evolution of the (modulationally unstable) state from the upper bifurcation branch with $\eta = 0.02$ (b). The solution diverges with time. Other parameters are the same as in Fig. 5 except $\epsilon = 0.1$.

in particular, manifested in the growth of a multiplicity of stationary solutions, as shown in Fig. 5(f).

VII. TEMPORAL CAVITY SOLITONS

In this section, we investigate numerically TCS solutions of the NDDE models using the RADAR5 code written in FORTRAN [50]. We start with the delay time $\tau = 25$ and the parameter values close to the LLE limit defined by Eqs. (15) and (18), $\kappa = e^{-2\epsilon^2}$, $\alpha = \epsilon^2$, $a = \epsilon$, $b = \epsilon^2$, $\theta = -3.5\epsilon^2$, $\eta = 1.855\epsilon^2$ with $\epsilon = 0.02$. The calculated TCS solution of Eq. (1) is shown in Fig. 7(a) by a black line. This soliton is very close to the TCS of the model (7) shown by a green line. The dissipative soliton of the LLE (19) is indicated by a red dashed line in the same figure for the LLE parameter values obtained using the relations (15) and (18), $\Theta = 3.5$, $\chi = 1$,

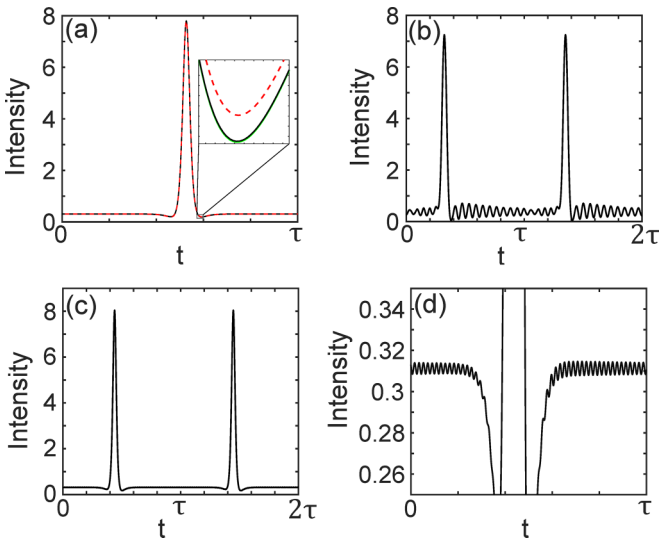


FIG. 7. TCS profiles calculated using the model equations (1) (black line) with $\epsilon = 0.02$ (a), $\epsilon = 0.34$ (b), $\epsilon = 0.1$ (c) and (d). Other parameters are given in the text. One can see from panel (d) that already for $\epsilon = 0.1$ the TCS tails exhibit a Cherenkov radiation, which is more pronounced at the trailing tail. In panel (a) the TCS of Eq. (7) is shown by a green line, and the soliton of the LLE (19) is shown by a red dashed line. Parameters are $\kappa = e^{-2\epsilon^2}$, $\alpha = \epsilon^2$, $a = \epsilon$, $b = \epsilon^2$, $\theta = -3.5\epsilon^2$, and $\eta = 1.855\epsilon^2$.

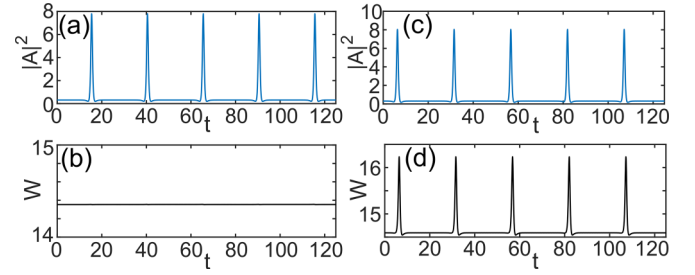


FIG. 8. Soliton propagation in Eq. (1) with $a = \epsilon$, $b = \epsilon^2$, $\theta = -3.5\epsilon^2$, $\epsilon = 0.02$, $\alpha = \epsilon^2$, $\kappa = e^{-2\epsilon^2}$, $\eta = 1.855\epsilon^2$, $\tau = 25$ (a). Corresponding to (a) quantity $W(t)$ (b). TCS profile of Eq. (1) calculated with $\epsilon = 0.2$ (c). Dynamics of a corresponding quantity $W(t)$ (d).

$b = 1$, $r = 1.855$ in Eq. (19). With increasing ϵ , the soliton profile gets more asymmetric; see Figs. 7(c) and 7(d) obtained with $\epsilon = 0.1$. As is seen in Fig. 7(d), the soliton tails exhibit slowly decaying oscillations, which can be attributed to the so-called Cherenkov radiation induced by high-order dispersion [42,43]. The Cherenkov radiation amplitude increases with ϵ , see Fig. 7(b) obtained with $\epsilon = 0.34$ and eventually destroys the TCS.

The time dependence of the quantity $W(t)$ from Eq. (2) calculated on the TCSs solutions of nonconservative Eq. (1) with $\kappa \neq 1$ and $\eta \neq 0$ is shown in Fig. 8. It is seen that for small $\epsilon = 0.02$ similarly to the conservative case, this quantity remains almost constant, while for larger $\epsilon = 0.2$ the time trace of $W(t)$ demonstrates short peaks similar to those in the intensity time trace.

The dependence of the TCS peak power on the parameter ϵ calculated using the models (1) (black line) and (7) (blue line) with exponential nonlinearity, and the model (12) (red line) with cubic nonlinearity, is shown in Fig. 9(a). It is seen that while sufficiently close to the LLE limit, $\epsilon \rightarrow 0$, this dependence looks rather smooth, it becomes fast oscillating with the increase of ϵ . Such oscillatory behavior can be explained by the interaction of a TCS with its own tails leading either to constructive or destructive interference due to the presence of

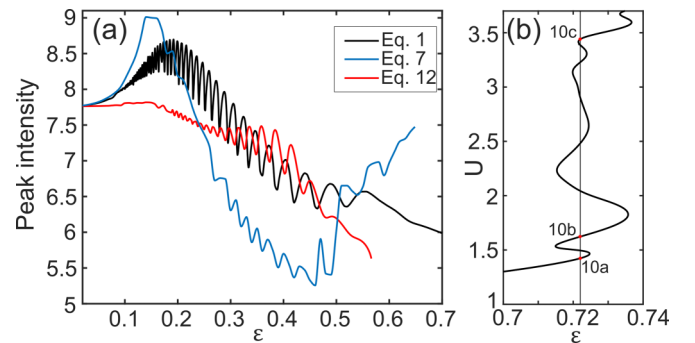


FIG. 9. TCS peak power as a function of the parameter ϵ calculated using Eq. (1) (black), Eq. (7) (blue), and Eq. (12) (red) with $\eta = 1.855\epsilon^2$ and $\tau = 25$ (a). Other parameters are the same as in Fig. 7. Continuation of the black curve from (a) in ϵ - U plane, where $U = \int_t^{t+\tau} |A|^2 dx$ (b). Points 10a, 10b, and 10c correspond to the solutions shown in Fig. 10. The branches with negative slope are dynamically unstable.

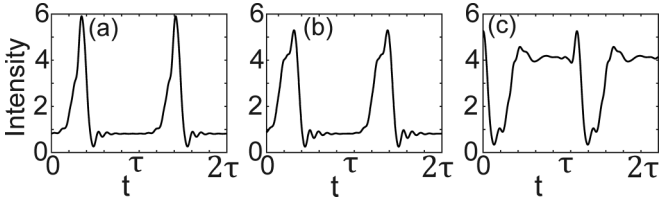


FIG. 10. Different types of stable localized solutions of the NDDE model (1) calculated for $\epsilon = 0.722$. The TCS shown in panel (a) corresponds to the black curve shown in Fig. 9. Other parameters are the same as in Fig. 7.

the Cherenkov radiation. Furthermore, it is seen that the oscillation frequency increases with the decrease of ϵ , which is in agreement with the fact that the frequency of the Cherenkov radiation tends to infinity when the third and/or fourth-order dispersion coefficients tend to zero; see, e.g., [51,52]. Note, that the model (7) demonstrates smaller oscillations of the TCS peak power with the increase of the parameter ϵ than Eq. (1). Since this model was obtained without neglecting $O(\alpha a)$ and $O(\alpha b)$ terms, it might be more suitable for the description of the Kerr cavity dynamics far away from the LLE and large delay limits.

At relatively high values of ϵ different types of localized solutions can appear, as is shown in Fig. 10, where the solutions shown in panels (a), (b), and (c) correspond to points 10a, 10b, and 10c in Fig. 9(b). It is seen from this figure that at large ϵ the evolution of the soliton solution branch has some similarity to the snaking behavior.

It is known that the soliton of the LLE can undergo an oscillatory instability with the increase of the injection. The NDDE model (1) also shows a similar behavior. Figure 11 illustrates the appearance of undamped oscillations of the soliton peak power for fixed relatively small $\epsilon = 0.05$. At higher values of ϵ there are different types of oscillating TCSs.

Similarly to LLE, the NDDE model does not contain any spectral filtering. To introduce it into the model let us assume that a Lorentzian spectral filter is placed between the two dispersive elements in Fig. 1(b). This filter is described by the relation

$$d\partial_t A(t) + A(t) = B(t), \quad (30)$$

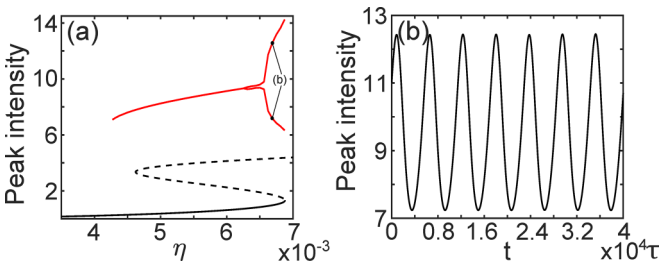


FIG. 11. TCS peak power (red curve) and intensity of CW solution (black curve) as functions of the injection η (a). The TCS starts to oscillate above the Andronov-Hopf bifurcation threshold at $\eta \approx 6.25 \times 10^{-3}$. Red lines show maximal and minimal peak power within the oscillation period. Time-trace of the TCS peak power calculated for $\eta = 6.7 \times 10^{-3}$ (b). $\epsilon = 0.05$. Other parameters are the same as in Fig. 7.

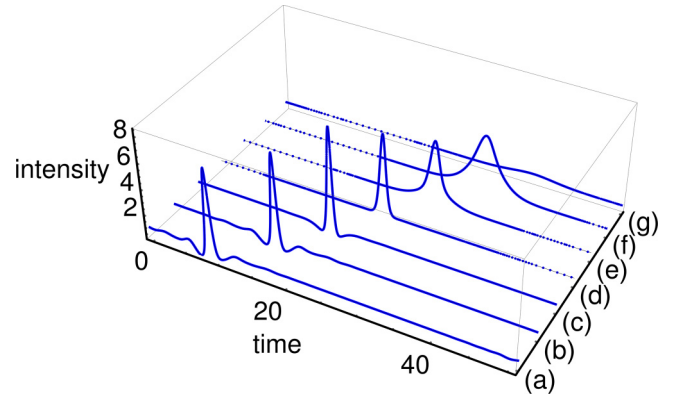


FIG. 12. Soliton solutions of Eq. (32) with different values of the inverse spectral filter width d . (a), (b), (c), (d), (e), (f), and (g) correspond to $d = 0.0, 0.1, 0.5, 1.0, 1.5, 2.0,$ and 2.5 , respectively. $\epsilon = 0.05$ and $\tau = 50$; other parameters are the same as in Fig. 7.

where A is the output field envelope, B is the input field envelope, and d is the inverse width of the filter. Here for simplicity it is assumed that the central frequency of the filter coincides with the injection frequency. Next, repeating the derivation of Eq. (1) given in Sec. III we obtain Eq. (10) with A_1 replaced by A and Eq. (11) with A_1 replaced by B . Combining these two equations, we get

$$\begin{aligned} & \left(B + a\partial_t B + \frac{a^2 - ib}{2} \partial_{tt} B \right) e^{-i\alpha|A|^2/2 - i\theta/2} \\ &= \sqrt{\kappa} \left(A_\tau - a\partial_t A_\tau + \frac{a^2 + ib}{2} \partial_{tt} A_\tau \right) e^{i\alpha|A_\tau|^2/2 + i\theta/2} + \eta. \end{aligned} \quad (31)$$

Using the multiscale method described in Sec. IV in the large delay and small dissipation limit, Eqs. (30) and (31) can be reduced to the LLE (19) with the additional diffusion term $(d^2/2)\partial_{t_0 t_0} u$ responsible for the spectral filtering. Substituting B from Eq. (30) into Eq. (31), we get an equation with nondelayed first, second, and third derivatives, $\partial_t A \equiv Y$, $\partial_{tt} A \equiv Z$, and $\partial_{ttt} A(t) \equiv \partial_t Z$, on the left-hand side, and first and second delayed derivatives $\partial_t A_\tau \equiv Y_\tau$ and $\partial_{tt} A_\tau \equiv Z_\tau$ on the right-hand side. Solving this equation with respect to nondelayed third derivative, $\partial_{ttt} A(t) \equiv \partial_t Z$, we get a system of three standard (non-neutral) DDEs:

$$\begin{aligned} \partial_t A = Y, \quad \partial_t Y = Z, \quad d\partial_t Z = \frac{2}{a^2 - ib} \left\{ \left[\sqrt{\kappa}(A_\tau - aY_\tau \right. \right. \\ \left. \left. + \frac{a^2 + ib}{2} Z_\tau \right) e^{i\alpha|A_\tau|^2/2 + i\theta} + \eta e^{i\theta/2} \right] e^{i\alpha|A + dY|^2/2} \\ \left. - \left[A + (a + d)Y + \frac{a^2 + 2ad - ib}{2} Z \right] \right\}. \end{aligned} \quad (32)$$

In the absence of spectral filtering, $d = 0$, the last equation in Eq. (32) is transformed into a delay algebraic equation. Thus, Eq. (32) becomes a system of delay differential-algebraic equations, which is equivalent to the NDDE model (1). The effect of the spectral filtering on the TCS solution of Eq. (32) is illustrated by Fig. 12. It is seen from this figure that for moderate values of $d \leq 0.5$ the spectral filtering suppresses

Cherenkov radiation without changing considerably the shape of the soliton itself. When the parameter d is further increased, the soliton width (peak power) starts to increase (decrease).

VIII. CONCLUSION

To conclude, we have developed a second-order NDDE model of a ring dispersive Kerr cavity subject to a coherent optical injection. Similarly to the first-order NDDE model discussed in [39] in the nondissipative limit, this model is reversible and has a conserved quantity. In a certain parameter range and under the mean-field and large delay approximations, the NDDE model can be reduced to the famous LLE model. However, unlike the LLE and similarly to the infinitely dimensional Ikeda map [40] and generalized LLE [19] Kerr cavity models, the NDDE model is able to describe the overlap of the resonances associated with different cavity modes. We have shown that TCSs can exist in the NDDE model not only close to the LLE limit, but also beyond this limit. In the latter case, they are strongly affected by the Cherenkov radiation, which is induced by high-order dispersion and eventually destroys the TCS. An important advantage of the NDDE model is that it can be analyzed numerically using standard codes, such as RADAR5 [50] and DDE-biftool [53]. Furthermore, after appropriate modifications this model can

be applied to study the effect of chromatic dispersion on the dynamics of mode-locked lasers and other laser systems. The NDDE model might be also useful for the consideration of the coupled-cavity systems, such as an optical microcavity pumped by a semiconductor mode-locked laser modeled by the DDE mode-locking model [23–25]. Furthermore, the NDDE model can be easily extended by including higher-order derivative terms into it. We have shown that by inserting a Lorentzian spectral filter into the cavity, the NDDE model can be converted into a standard DDE. Similarly, other intracavity elements such as amplifying and absorbing media can be considered when deriving the model equations. Thus, the approach to modeling the intracavity dispersion proposed in this paper can be applied not only to describe the dynamics of Kerr resonators, but also to study the effect of dispersion on the dynamics of a wide class of laser systems.

ACKNOWLEDGMENTS

Stimulating discussions with Guillaume Huyet, Dmitry Turaev, Sergei Turitsyn, Matthias Wolfrum, and Thomas Seidel as well as the support by the Deutsche Forschungsgemeinschaft (DFG Projects No. 445430311 and No. 491234846) are gratefully acknowledged.

-
- [1] S. T. Cundiff and J. Ye, *Rev. Mod. Phys.* **75**, 325 (2003).
 - [2] J. Schröder, A. Fülöp, M. Mazur, L. Lundberg, Ó. B. Helgason, M. Karlsson, P. A. Andrekson *et al.*, *J. Lightwave Technol.* **37**, 1663 (2019).
 - [3] N. Picqué and T. W. Hänsch, *Nat. Photon.* **13**, 146 (2019).
 - [4] M.-G. Suh, X. Yi, Y.-H. Lai, S. Leifer, I. S. Grudin, G. Vasisht, E. C. Martin, M. P. Fitzgerald, G. Doppmann, J. Wang *et al.*, *Nat. Photon.* **13**, 25 (2019).
 - [5] P. Trocha, M. Karpov, D. Ganin, M. H. Pfeiffer, A. Kordts, S. Wolf, J. Krockenberger, P. Marin-Palomo, C. Weimann, S. Randel *et al.*, *Science* **359**, 887 (2018).
 - [6] X. Xue and A. M. Weiner, *Front. Optoelectron.* **9**, 238 (2016).
 - [7] D. J. Jones, S. A. Diddams, J. K. Ranka, A. Stentz, R. S. Windeler, J. L. Hall, and S. T. Cundiff, *Science* **288**, 635 (2000).
 - [8] P. Del’Haye, A. Schliesser, O. Arcizet, T. Wilken, R. Holzwarth, and T. J. Kippenberg, *Nature (London)* **450**, 1214 (2007).
 - [9] A. Parriaux, K. Hammani, and G. Millot, *Adv. Opt. Photon.* **12**, 223 (2020).
 - [10] K. Ikeda, *Opt. Commun.* **30**, 257 (1979).
 - [11] L. A. Lugiato and R. Lefever, *Phys. Rev. Lett.* **58**, 2209 (1987).
 - [12] F. Leo, S. Coen, P. Kockaert, S.-P. Gorza, P. Emplit, and M. Haelterman, *Nat. Photon.* **4**, 471 (2010).
 - [13] P. Grelu and N. Akhmediev, *Nat. Photon.* **6**, 84 (2012).
 - [14] T. Herr, V. Brasch, J. D. Jost, C. Y. Wang, N. M. Kondratiev, M. L. Gorodetsky, and T. J. Kippenberg, *Nat. Photon.* **8**, 145 (2014).
 - [15] Y. K. Chembo and C. R. Menyuk, *Phys. Rev. A* **87**, 053852 (2013).
 - [16] S. Coen and M. Haelterman, *Phys. Rev. Lett.* **79**, 4139 (1997).
 - [17] K. J. Blow and N. J. Doran, *Phys. Rev. Lett.* **52**, 526 (1984).
 - [18] T. Hansson and S. Wabnitz, *J. Opt. Soc. Am. B* **32**, 1259 (2015).
 - [19] Y. Kartashov, O. Alexander, and D. Skryabin, *Opt. Express* **25**, 11550 (2017).
 - [20] M. Conforti and F. Biancalana, *Opt. Lett.* **42**, 3666 (2017).
 - [21] M. Anderson, Y. Wang, F. Leo, S. Coen, M. Erkintalo, and S. G. Murdoch, *Phys. Rev. X* **7**, 031031 (2017).
 - [22] A. V. Cherenkov, V. E. Lobanov, and M. L. Gorodetsky, *Phys. Rev. A* **95**, 033810 (2017).
 - [23] A. G. Vladimirov and D. Turaev, *Phys. Rev. A* **72**, 033808 (2005).
 - [24] A. G. Vladimirov, D. Turaev, and G. Kozyreff, *Opt. Lett.* **29**, 1221 (2004).
 - [25] A. G. Vladimirov and D. Turaev, *Radiophys. Quantum Electron.* **47**, 769 (2004).
 - [26] E. A. Viktorov, P. Mandel, A. G. Vladimirov, and U. Bandelow, *Appl. Phys. Lett.* **88**, 201102 (2006).
 - [27] R. Lang and K. Kobayashi, *IEEE J. Quantum Electron.* **16**, 347 (1980).
 - [28] M. C. Soriano, J. García-Ojalvo, C. R. Mirasso, and I. Fischer, *Rev. Mod. Phys.* **85**, 421 (2013).
 - [29] J. Mulet and S. Balle, *IEEE J. Quantum Electron.* **41**, 1148 (2005).
 - [30] A. G. Vladimirov, S. Suchkov, G. Huyet, and S. K. Turitsyn, *Phys. Rev. A* **104**, 033525 (2021).
 - [31] E. A. Viktorov, P. Mandel, and G. Huyet, *Opt. Lett.* **32**, 1268 (2007).
 - [32] S. Slepneva, B. Kelleher, B. O’Shaughnessy, S. P. Hegarty, A. G. Vladimirov, and G. Huyet, *Opt. Express* **21**, 19240 (2013).
 - [33] M. Heuck, S. Blaaberg, and J. Mørk, *Opt. Express* **18**, 18003 (2010).

- [34] A. Pimenov, S. Slepneva, G. Huyet, and A. G. Vladimirov, *Phys. Rev. Lett.* **118**, 193901 (2017).
- [35] C. Schelte, P. Camelin, M. Marconi, A. Garnache, G. Huyet, G. Beaudoin, I. Sagnes, M. Giudici, J. Javaloyes, and S. V. Gurevich, *Phys. Rev. Lett.* **123**, 043902 (2019).
- [36] C. Schelte, D. Hessel, J. Javaloyes, and S. V. Gurevich, *Phys. Rev. Appl.* **13**, 054050 (2020).
- [37] A. Pimenov, S. Amiranashvili, and A. G. Vladimirov, *Math. Model. Nat. Phenom.* **15**, 47 (2020).
- [38] A. Pimenov and A. G. Vladimirov, *Optics* **3**, 364 (2022).
- [39] T. G. Seidel, S. V. Gurevich, and J. Javaloyes, *Phys. Rev. Lett.* **128**, 083901 (2022).
- [40] M. Haelterman, S. Trillo, and S. Wabnitz, *Opt. Commun.* **91**, 401 (1992).
- [41] T. Kolokolnikov, M. Nizette, T. Erneux, N. Joly, and S. Bielawski, *Physica D* **219**, 13 (2006).
- [42] V. I. Karpman, *Phys. Rev. E* **47**, 2073 (1993).
- [43] N. Akhmediev and M. Karlsson, *Phys. Rev. A* **51**, 2602 (1995).
- [44] P. K. A. Wai, H. H. Chen, and Y. C. Lee, *Phys. Rev. A* **41**, 426 (1990).
- [45] J. Elgin, *Opt. Lett.* **17**, 1409 (1992).
- [46] J. P. Gordon, *J. Opt. Soc. Am. B* **9**, 91 (1992).
- [47] D. G. Rabus and C. Sada, *Integrated Ring Resonators*, Springer Series in Optical Sciences (Springer Nature, Switzerland, 2020), Vol. 127.
- [48] S. Yanchuk and M. Wolfrum, *SIAM J. Appl. Dyn. Syst.* **9**, 519 (2010).
- [49] C. Godey, I. V. Balakireva, A. Coillet, and Y. K. Chembo, *Phys. Rev. A* **89**, 063814 (2014).
- [50] N. Guglielmi and E. Hairer, *Computing* **67**, 1 (2001).
- [51] A. G. Vladimirov, S. V. Gurevich, and M. Tlidi, *Phys. Rev. A* **97**, 013816 (2018).
- [52] A. G. Vladimirov, M. Tlidi, and M. Taki, *Phys. Rev. A* **103**, 063505 (2021).
- [53] K. Engelborghs, T. Luzyanina, and G. Samaey, DDE-biftool v.2.00: A matlab package for bifurcation analysis of delay differential equations, Tech. Rep. TW-330 (Department of Computer Science, K.U. Leuven, Leuven, Belgium, 2001).